WATER RESOURCES RESEARCH, VOL. 43, W03438, doi:10.1029/2006WR005324, 2007

Miscible displacement fronts of shear thinning fluids inside rough fractures

A. Boschan,[1,2] H. Auradou,[1] I. Ippolito,[2] R. Chertcoff,[2] and J. P. Hulin[1]

Received 10 July 2006; revised 27 October 2006; accepted 7 November 2006; published 27 March 2007.

[1] The miscible displacement of a shear-thinning fluid by another fluid with the same rheological properties is studied experimentally in a transparent fracture by an optical technique that images relative concentration distributions. The fracture walls have complementary self-affine geometries and are shifted laterally in the direction perpendicular to the mean flow velocity **U**: The flow field is strongly channelized and macrodispersion controls the front structure for Péclet numbers above a few units. The global front width increases therefore linearly with time and reflects the velocity distribution between the different channels. In contrast, at the local scale, front spreading is similar to Taylor dispersion between plane-parallel surfaces. Both dispersion mechanisms depend strongly on the fluid rheology, which shifts from Newtonian to shear thinning when the flow rate increases. In the latter domain, increasing the concentration enhances the global front width but reduces both Taylor dispersion (due to the flattening of the velocity profile in the gap of the fracture) and the size of medium scale front structures.

Citation: Boschan, A., H. Auradou, I. Ippolito, R. Chertcoff, and J. P. Hulin (2007), Miscible displacement fronts of shear thinning fluids inside rough fractures, *Water Resour. Res.*, *43*, W03438, doi:10.1029/2006WR005324.

1. Introduction

[2] The transport of dissolved species in fractured formations is of primary importance in a large number of groundwater systems: predicting the migration rate and the dispersion of contaminants from a source inside or at the surface of a fractured rock is then relevant to many fields such as waste storage and water management [*NAS Committee on Fracture Characterization and Fluid Flow*, 1996; *Adler and Thovert*, 1999; *Berkowitz*, 2002].

[3] In the present work, these phenomena are studied experimentally by analyzing relative concentration distributions during the displacement of a transparent fluid by a miscible dyed one inside a model transparent rough fracture. A key characteristic of these fractures is the self-affine geometry of their wall surfaces: it reproduces the multiscale geometrical characteristics of many faults and "fresh" fractures. For such surfaces, the variance $\Delta h^2 = < (h(\vec{r} + \vec{\Delta r}) - h(\vec{r}))^2 >$ of the local height $h(x, y)$ of the surface with respect to a reference plane satisfies:

$$\frac{\Delta h}{l} = \left(\frac{\Delta r}{l}\right)^{\zeta}, \tag{1}$$

in which (x, y) are coordinates in the plane of the fracture, ζ is the self-affine exponent, l the topothesy (i.e., the length scale at which the slope $\Delta h/\Delta r$ is of the order of 1).

[4] In this work, the rough fracture walls have complementary geometries: they are separated by a small distance normal to their mean plane and shifted laterally relative to each other. This shear displacement induces local aperture variations: experimental and numerical investigations demonstrate that, in this case, preferential flow paths dominantly perpendicular to the shear appear [*Gentier et al.*, 1997; *Yeo et al.*, 1998; *Auradou et al.*, 2005]. These paths strongly influence fluid transport [*Neretnieks et al.*, 1982; *Tsang and Tsang*, 1987; *Brown et al.*, 1998; *Becker and Shapiro*, 2000], particularly when the mean flow is, as here, parallel to these channels.

[5] The objective of the present paper is to study the influence of the structure of the aperture field on the displacement front of a transparent fluid by a dyed miscible one. For that purpose, the displacement process is studied at different length scales in order to identify the different front spreading mechanisms. Practically, the displacement front is analyzed in regions of interest of variable widths W perpendicular to the flow. If W is smaller than the local fracture aperture, the front spreading will be dispersive and controlled by local mechanisms; for large W values of the order of transverse size of the fracture (100 times the aperture) the front structure is controlled, on the contrary, by preferential flow paths. Additional information on these mechanisms will be obtained from the influence of the flow velocity and of the fluid rheology (for instance, velocity contrasts between preferential flow paths and slower flow zones may be varied by using shear thinning fluids of different concentrations).

2. Dispersion and Front Spreading in Rough Fractures

[6] Previous studies by *Ippolito et al.* [1993], *Roux et al.* [1998], *Adler and Thovert* [1999], and *Detwiler et al.*

[1]Laboratoire Fluides, Automatique et Systèmes Thermiques, UMR 7608, CNRS, Université Paris 6 and 11, Orsay, France.
[2]Grupo de Medios Porosos, Facultad de Ingeniería, Universidad de Buenos Aires, Buenos Aires, Argentina.

0043-1397/07/2006WR005324$09.00

[2000] described mixing in fractures by a Gaussian convection-dispersion equation. They suggested that the dispersion coefficient is the sum of the contributions of geometrical and Taylor dispersion. The latter results from the local advection velocity gradient between the walls of the fracture: its influence is balanced by molecular diffusion across the gap. There results a macroscopic Fickian dispersion parallel to the flow [*Taylor*, 1953; *Aris*, 1956] characterized by the coefficient:

$$\frac{D}{D_m} = \tau + f\,Pe^2, \tag{2}$$

where D_m is the molecular diffusion coefficient, the Péclet number $Pe = Ua_0/D_m$ represents the relative influence of the velocity gradients and molecular diffusion, U the average flow velocity in the whole fracture, a the gap thickness, τ the tortuosity of the void space reducing the rate of longitudinal molecular diffusion [*Bear*, 1972; *Drazer and Koplik*, 2002]; for flat parallel plates and a Newtonian fluid, $f = 1/210$.

[7] Geometrical dispersion reflects the disorder of the velocity field in the fracture plane and may be significant in rough fractures. Theoretical investigations by [*Roux et al.*, 1998] suggest that this geometrical mechanism is important at intermediate *Pe* values; at lower (higher) Péclet numbers, molecular diffusion (Taylor dispersion) are dominant. Scaling arguments allow in addition to estimate Péclet numbers corresponding to the limits of these domains: they depend on the mean, the variance and the correlation length of the aperture field. Such predictions are supported by experimental investigations on model fractures with a relatively weak disorder of the aperture field [*Ippolito et al.*, 1993, 1994; *Adler and Thovert*, 1999; *Detwiler et al.*, 2000].

[8] In natural fractures, however, experimental [*Neretnieks et al.*, 1982; *Brown et al.*, 1998; *Becker and Shapiro*, 2000] and numerical [*Drazer et al.*, 2004] studies indicate that mass transport is strongly influenced by large scale preferential flow channels parallel to the mean velocity. Anomalous dispersion is then expected as in the analogous case of porous media with strata of different permeabilities [*Matheron and de Marsily*, 1980]. As pointed out by *Roux et al.* [1998], similar effects are expected in fractures if the flow velocities vary slower along a streamline than perpendicular to it. Then, large distortions of the displacement front [*Drazer et al.*, 2004] may appear and grow linearly with time. Moreover, in highly distorted parts of the front, transverse concentration gradients appear and induce a transverse tracer flux that further enhances dispersion.

[9] Another important parameter influencing miscible displacements is the rheology of the flowing fluids (relevant, for instance, to enhanced oil recovery using polymer solutions [*Bird et al.*, 1987]. Nonlinear rheological properties modify indeed the flow velocity field and, more specifically, the flow velocity contrasts [*Sahimi*, 1993; *Shah and Yortsos*, 1995; *Fadili et al.*, 2002]. In the case of shear-thinning fluids in simple geometries like tubes or parallel plates, the flow profile is no longer parabolic but flattens in the center part of the flow channels where the shear rate is lowest: this decreases the dispersion coefficient (compared to the Newtonian case) but the square law variation of the dispersion coefficient with the Péclet number is still satisfied. For instance, when the viscosity μ varies with the shear rate $\dot{\gamma}$ following a power law: $\mu \propto \dot{\gamma}^{n-1}$, equation (2) remains valid but f is a function of n [*Vartuli et al.*, 1995].

[10] In heterogeneous media, on the contrary, numerical investigations suggest that the flow of shear thinning fluids gets concentrated in a smaller number of preferential flow paths than for Newtonian ones [*Shah and Yortsos*, 1995; *Fadili et al.*, 2002]: the macrodispersion reflecting large-scale distortions of the displacement front is then increased (even though the local dispersion due to the flow profile in individual channels is reduced). Finally, in this work and in contrast with oil recovery, the polymer concentration in the injected and displaced fluids is the same: we investigate only its influence on the transport of a passive solute. The influence of the shear thinning properties is studied by running experiments with different polymer concentrations.

3. Experimental Setup and Procedure

3.1. Model Fractures and Fluid Injection Setup

[11] Model fractures used in the present work are made of two complementary transparent rough self-affine surfaces clamped together. A self-affine surface is first generated numerically using the midpoint algorithm [*Feder*, 1988] with a self-affine exponent ζ equal to the value 0.8 measured for many materials, including granite [*Bouchaud*, 2003]. Using a surface generated numerically avoids the possible influence of unwanted macroscopic defects which would distort the results if surface scans of natural samples were used. Then, the surfaces are carved by a computer controlled milling machine into a parallelepiped Plexiglas block. The final steps of the machining require an hemispherical tool with a 600 μm diameter. The effective size of the surface is 171 by 85 mm and the difference in height between the lowest and highest points of the surface is 19.2 mm while the mean square deviation of the height is 3 mm. The two surfaces are exactly complementary except for a 0.33 mm relative shift parallel to their length; they are bounded on their larger sides by 10 mm wide borders rising slightly above the surfaces. The geometry of these borders is chosen so that they match perfectly and act as spacers leaving an average mean distance $a_0 = 0.75$ mm between the surfaces when the blocks are clamped together. The standard deviation of the aperture is $\sigma = 0.11$ mm; the values of its semivariance [*Kitanidis*, 1997] normalized by $2\sigma^2$ are 0.6 (0.8) for distances equal to a_0 and parallel and perpendicular, respectively, to the length of the model. The difference between these two last values reflects an anisotropy of the aperture field. In all cases, the gap between the surfaces is large enough so that the two walls do not touch: both the mean aperture a_0 and the relative displacement are the same in all experiments. Avoiding mechanical contact points allows to develop more complete and simpler interpretations due to the narrower distribution of the transit times through the different regions of the fracture. Such models describe well artificial fractures created, for instance, during the stimulation of oil wells and which are kept open thereafter by proppant particles.

[12] The fracture assembly is positioned vertically (Figure 1a) with the two vertical sides (corresponding to the borders) sealed while the two others are open. The upper side of the model is connected to a syringe pump sucking

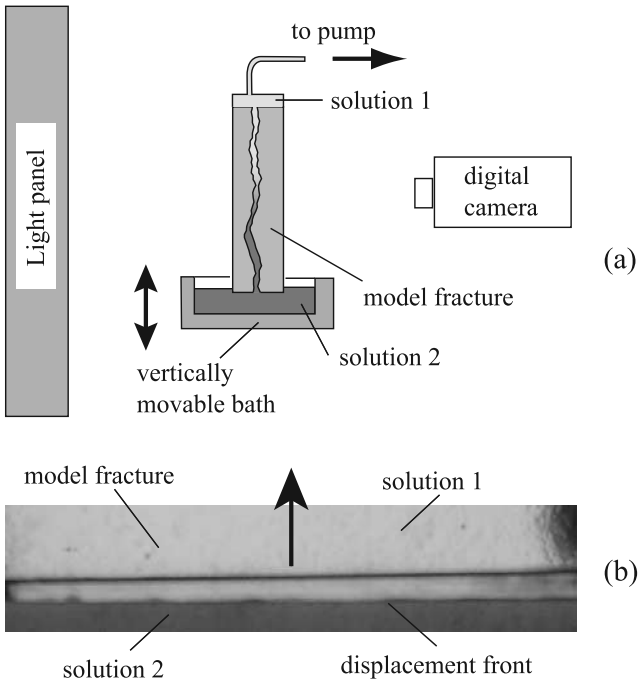

Figure 1. (a) Schematic side view of the experimental setup. (b) Front close-up view of the setup as the front of dyed fluid just penetrates into the model. The dark line above the front and parallel to it is the rim of the walls of the outside bath.

the fluids upward out of the fracture. The lower horizontal side is dipped into a reservoir which may be moved up and down. The fracture is first saturated by sucking fluid out of the lower reservoir into the model. Then, the original fluid is replaced by the other after lowering the reservoir before raising it again and starting the displacement experiment by pumping fluid at the top of the model. This procedure avoids unwanted intrusions while replacing a fluid by the other and allows to purge completely the lower reservoir; a perfectly straight front between the injected and displaced fluids is obtained in this way at the onset of the experiment (Figure 1b).

3.2. Fluid Preparation and Characteristics

[13] In all experiments, the injected and displaced fluids are identical water-scleroglucan solutions but for a small amount of Water Blue dye [*Horobin and Kiernan*, 2002] added to one of the solutions at a mass concentration c_0 = 0.3 g/L. A similar amount of *NaCl* is added to the other solution in order to keep both densities equal within $\pm 1 \times 10^{-4}$ (the density values are checked by an Anton-Paar *DMA*35 oscillating tube densimeter). The dye has been chosen such that it has no physicochemical interaction with the model walls and can be considered as a passive tracer. The molecular diffusion coefficient of the dye $D_m \simeq 6.5 \times 10^{-10}$ m^2 s^{-1} is determined independently from Taylor dispersion measurements in a capillary tube.

[14] The rheological properties of the scleroglucan solutions have been characterized using a Contraves LS30 Couette rheometer in range of shear rates $0.016\ \mathrm{s}^{-1} \leq \dot{\gamma} \leq 87\ \mathrm{s}^{-1}$. The rheological properties of the solutions have been verified to be constant with time within experimental error (over a time lapse of 3 days) and to be identical for the dyed and transparent solutions (for a same polymer concentrations). The variation of the viscosity η with $\dot{\gamma}$ is well fitted by the classical Carreau formula:

$$\eta = \frac{\eta_0 - \eta_\infty}{\left(1 + \left(\frac{\dot{\gamma}}{\dot{\gamma}_0}\right)^2\right)^{\frac{1-n}{2}}} + \eta_\infty. \tag{3}$$

The values of these rheological parameters for the polymer solutions used in the present work are listed in Table 1. The parameter η_∞ is taken equal to the value of the solvent viscosity (10^{-3} Pa s for water) since its determination would require measurements beyond the experimental range limited to $\dot{\gamma} = 87\ \mathrm{s}^{-1}$. In equation (3), $\dot{\gamma}_0$ corresponds to a crossover between two regimes. For $\dot{\gamma} < \dot{\gamma}_0$, the viscosity η tends to η_0, and the fluid behaves as a Newtonian fluid. On the other hand, for $\dot{\gamma} > \dot{\gamma}_0$, η decreases following a power law $\mu \propto \dot{\gamma}^{(n-1)}$. Note that, due to the small volume fraction of polymer, the molecular diffusion coefficient keeps the same value as in pure water.

3.3. Optical Relative Concentration Measurements

[15] The flow rate is kept constant during each experiment and ranges between 0.01 and 1 mL/min. The total duration of the experiments in order to obtain a complete saturation of the fracture by the invading fluid varies between 20 min and 33 hours. The transparent fracture is back illuminated by a light panel: about 100 images of the distribution of light transmitted through the fracture are recorded at constant intervals during the fluid displacement using a Roper Coolsnap HQ digital camera with a high, 12 bits, dynamic range. Reference images are recorded both before the experiments and after the full saturation by the displacing fluid in order to have images corresponding to the fracture fully saturated with both the transparent and the dyed fluid.

[16] The local relative concentration of the displacing fluid (averaged over the fracture aperture) is determined from these images by the following procedure. First, the absorbance $A(x, y, t)$ of light by the dye on an image obtained at time t is computed by the relation:

$$A(x,y,t) = ln\left(\frac{I_t(x,y)}{I(x,y,t)}\right) \tag{4}$$

in which $I_t(x, y)$ and $I(x, y, t)$ are the transmitted light intensities (in gray levels) measured for a pixel of coordinates (x, y) respectively when the fracture is saturated with transparent fluid and at time t. When the fracture is saturated with the dyed fluid ($c(x, y) = c_0$), the transmitted light intensity is $I_0(x, y)$ and the adsorbance is:

$$A_0(x,y) = ln\left(\frac{I_t(x,y)}{I_0(x,y)}\right) \tag{5}$$

Table 1. Rheological Parameters of Scleroglucan Solutions Used in the Flow Experiments

Polymer Concentration, ppm	n	$\dot{\gamma}_0$, s^{-1}	η_0, mPa s
500	0.38 ± 0.04	0.077 ± 0.018	410 ± 33
1000	0.26 ± 0.02	0.026 ± 0.004	4490 ± 342

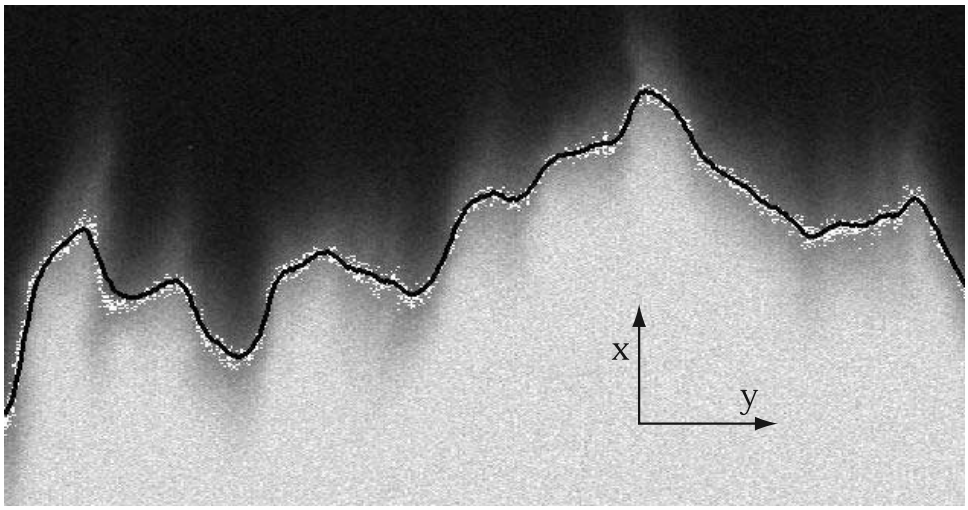

Figure 2. Experimental relative concentration field obtained with a 1000 ppm polymer concentration for a mean front displacement of half the fracture length. Gray levels represent values of the ratio $c(x, y, t)/c_0$. Size of field of view is 81 mm × 70 mm; only a part of the actual image is shown. Solid line shows front profile $x_f(y, t)$ as defined in section 6.1; white dots are pixels where $c(x, y, t)/c_0 = 0.5 \pm 0.03$.

The relation between the local concentration $c(x, y, t)$ (averaged over the local fracture aperture), the dye concentration c_0 in the dyed fluid and the absorbances A and A_0 has been determined independently from calibration pictures realized with the fracture saturated with dyed solutions of concentrations c increasing from 0.1 to 0.5 g/L. The ratio $A(x, y)/A_0(x, y)$ is found experimentally to be constant within ±3% over the picture area: for more precision, the ratio $< A >_{x,y}/< A_0 >_{x,y}$ of the averages is therefore used to determine the calibration curve. Because of nonlinear adsorbance [*Detwiler et al.*, 2000], the relation $c/c_0 = < A >_{x,y}/< A_0 >_{x,y}$ predicted by Beer-Lambert's law is not valid. In our experimental setup, the variation of c/c_0 with $< A >/< A_0 >$ was found experimentally to follow accurately the polynomial relation:

$$\frac{c}{c_0} = b_1 \frac{A}{A_0} + b_2 \left(\frac{A}{A_0}\right)^2 + b_3 \left(\frac{A}{A_0}\right)^3 \tag{6}$$

with $b_1 = 0.186 \pm 0.023$, $b_2 = 0.0087 \pm 0.04$ and $b_3 = 0.108 \pm 0.021$. The resulting global absolute uncertainty on the value of c/c_o (varying between 0 and 100%) is ±1.5%: this uncertainty reflects the cumulated effects of the variability of the local aperture of the fracture and of other sources of error. Practically, equation (6) is applied to all pixels (x, y) in the pictures recorded during the experiment in order to obtain $c(x, y, t)/c_0$. An instantaneous relative concentration map obtained in this way is displayed in Figure 2. In the following, c_0 is omitted and $c(x, y, t)$ refers to the local relative concentration at a given time averaged over the aperture.

4. Local Concentration Variations

[17] As already pointed above, transport in the fracture results from the combination of front spreading due to large-scale flow velocity variations and of mixing due to local dispersion mechanisms and concentration gradients. In order to identify these different processes, a local analysis is first performed. For each pixel (x, y), the variation $c(x, y, t)$ with time of the local relative concentration of the dyed fluid has been determined; as can be seen in Figure 3, it is well fitted by the following solution of the convection-dispersion equation corresponding to the stepwise concentration variations induced experimentally:

$$c(x,y) = \frac{1}{2}\left(1 + erf\,\frac{t - \overline{t(x,y)}}{\sqrt{4\dfrac{D(x,y)}{U^2}t}}\right) \tag{7}$$

In equation (7), U is the mean velocity, $\overline{t(x,y)}$ the mean transit time and $D(x, y)$ is an effective coefficient reflecting the cumulated dispersion along the streamline leading from the inlet side of the model to point (x, y) (all these quantities reflect averages over the aperture of the fracture). Note that, if

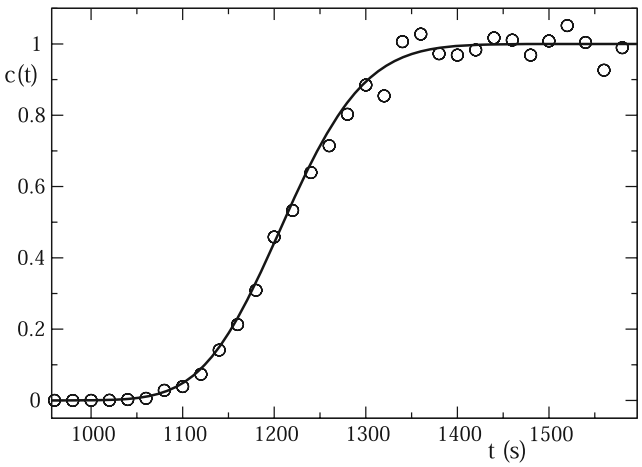

Figure 3. Time variation of the relative concentration $c(x, y, t)$ for $x = 20$ mm and $y = 36$ mm for 1000 ppm polymer solutions. Mean flow velocity $U = 0.014$ mm/s ($Pe = 150$). Circles are experimental data. Solid line is the fit by equation (7) with $\overline{t(x,y)} = 1212$ s and $D(x, y) = 0.315$ mm^2/s.

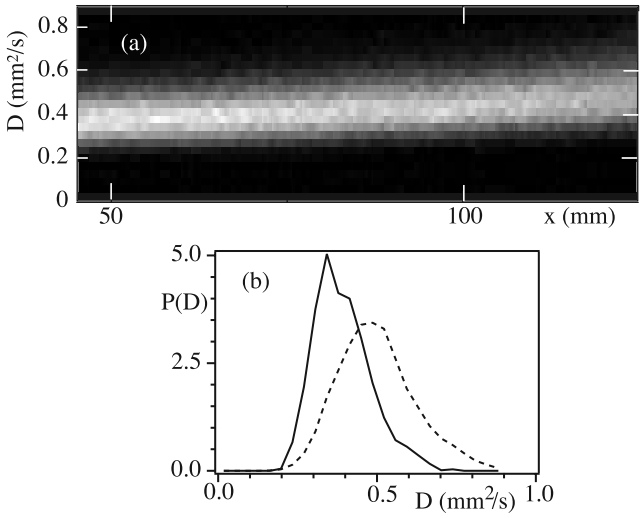

Figure 4. Probability distribution $P(D, x)$ of the dispersion coefficient for a dyed solution displacing a transparent one: mean flow velocity $U = 0.014$ mm/s ($Pe = 150$, polymer concentration 1000 ppm). Only data corresponding to distances $x \geq 45$ mm for which a clear dispersion regime is established and the concentration variations $c(x, y, t)$ well fitted by equation (7) are plotted. (a) Gray levels corresponding to the value of the probability P(D) at the corresponding values of D and x. (b) Distributions $P(D)$ for $x = 45$ (solid line) and 125 mm (dashed line).

the injected fluid is the transparent one, the plus sign should be replaced by a minus sign in equation (7). Both $D(x, y)$ and $t(x, y)$ depend on the measurement point (x, y).

[18] In the following, the variations of these quantities are analyzed: on the one hand, the spatial variations of $\bar{t}(x, y)$ reveal the channelized structure of the flow that leads to macrodispersion. On the other hand, we shall discuss now $D(x, y)$ which reflects local mixing processes taking place on each streamline.

5. Dispersive Mixing Along Individual Streamlines

[19] In this section, the variation of $D(x, y)$ is studied as a function of the distance x from the inlet and of the fluid velocity and rheology. The probability distribution of the values of $D(x, y)$ for all pixels at a same distance x for a given experiment is displayed in Figure 4a in a gray scale as a function of x ($45 \leq x \leq 125$ mm). Figure 4b shows the two extreme distributions corresponding to $x = 45$ (solid line) and 125 mm: one observes that the mean value $\bar{D}$ of the distributions weakly increases between $x = 45$ and 125 mm. In the following, $\bar{D}$ is referred to as D and the deviations of the local values are characterized by the width ΔD of $P(D)$ at midheight which increases also slowly with distance.

[20] The drift of D may be due to slow variations of the mean aperture and flow velocity. It reflects also the larger dispersion in distorted regions of the front observed in the fracture plane: there, dye diffuses across parallel streamlines of different velocities which contributes to broaden the front. The slow variation of the mean value of D with x, together with the good fit displayed in Figure 3, demonstrate that the Fickian dispersion model describes well the local spreading of the front throughout the experiment. The symmetry of the process is finally checked by realizing the same experiments with the transparent solution displacing the dyed one. The distributions of the dispersion coefficients for given values of x are the same as in the reverse configuration: there is therefore no effect of small residual density contrasts.

[21] The dependence of the local dispersion on the flow velocity U for the 500 ppm and 1000 ppm solutions is displayed in Figure 5 where D is plotted as a function of the Péclet number Pe defined above. The same trends are followed for both solutions: for low Pe values the dispersion coefficient tends toward a constant close to 1 while, at high Pe, D increases as the square of Pe. These variations are similar to the predictions of equation (2) also plotted in Figure 5 (solid, dotted, and dashed lines) for a Newtonian fluid and two power law shear thinning fluids for which $\mu \propto \dot{\gamma}^{n-1}$ (n is taken equal to the values listed in Table 1 and the value of f in equation (2) is computed from equation (4) of *Boschan et al.* [2003]). The overall agreement observed implies that Taylor dispersion is indeed the dominant mechanism controlling local dispersion.

[22] In a more detailed analysis, one must however take into account the fact that, for real fluids, the viscosity does not diverge at low shear rates but becomes constant (Newtonian plateau viscosity) for $\dot{\gamma} < \dot{\gamma}_0$. In a Poiseuille Newtonian flow between two parallel flat plates, the shear rate is maximum at the wall with $\dot{\gamma} = 6U/a$. It follows that the transition value $\dot{\gamma}_0$ is reached for $U = U_c = a\,\dot{\gamma}_0/6$. Using the values of $\dot{\gamma}_0$ in Table 1, the velocities U_c (Péclet numbers Pe_c) corresponding to the 500 ppm and 1000 ppm solutions are 0.01 mm/s and 0.003 mm/s ($Pe_c = 11$ and 4). Below Pe_c, the dispersion coefficient should be the same as for a Newtonian fluid; above Pe_c, its variation should progressively merge with that predicted for power law fluids. This crossover is clearly observed in Figure 5: for $Pe < 30$, the values of D obtained with the 500 ppm and 1000 ppm

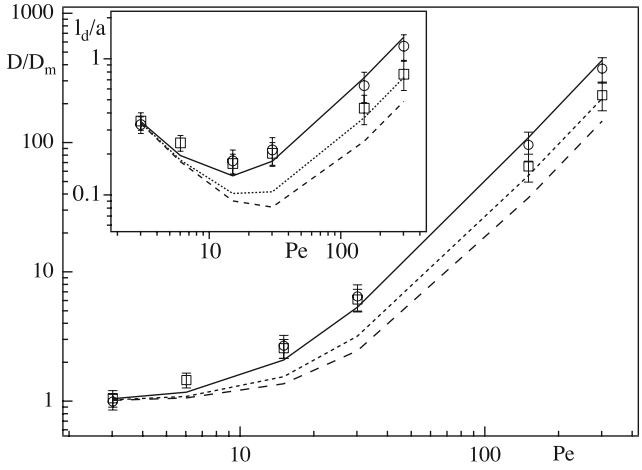

Figure 5. Variation of normalized dispersion coefficient D/D_m with $Pe = Ua_0/D_m$. Inset shows variation of the dispersivity $l_d = D/U$. Solid, dotted, and dashed lines show, respectively, predictions from equation (2) for $n = 1$ (Newtonian fluid), $n = 0.38$, and $n = 0.26$ (shear-thinning solutions with 500 ppm and 1000 ppm polymer concentrations, respectively).

Figure 6. Gray scale map of the normalized local transit time $\overline{t(x,y)}U/x$. Flow is from left to right. Dark (light) regions correspond to locations where $\overline{t(x,y)}U/x < 1$ ($\overline{t(x,y)}U/x > 1$). Mean flow velocity U = 0.014 mm/s (Pe = 150, polymer concentration 1000 ppm). The map covers the total area of the model fracture (size 85 × 171 mm).

solutions are the same and are close to the predictions for Newtonian fluids. At high Péclet numbers, data points corresponding to the two solutions get separated and the value of D corresponding to the 1000 ppm solution is lower than that for the 500 ppm one. The difference is of the same order of magnitude as the predictions for power law fluids with the corresponding values of n.

[23] It is often convenient to replace the dispersion coefficient D by the dispersivity $l_d = D/U$ to identify more easily the influence of spatial heterogeneities of the flow field. For Taylor like dispersion satisfying equation (2) and for a Newtonian fluid, the dispersivity has a minimum equal to $l_d = 2a/\sqrt{210} \approx 0.14a$ for $Pe = \sqrt{210} \simeq 14.5$. The inset of Figure 5 displays the variation of the dispersivity with Pe: its minimum value corresponds well to the theoretical prediction for Newtonian fluids (solid line). This confirms that, in this range of Péclet numbers, the two polymer solutions behave like Newtonian fluids.

[24] These results demonstrate that the dispersion $D(x, y)$ along individual streamlines in the rough model fracture is mainly due to the flow profile in the gap between the walls and similar to that between flat parallel plates. This is likely due to the specific properties of the flow field. First, as for parallel plates, some streamlines located close to the upper or lower wall will remain in their vicinity all along their path through the sample: as in Taylor dispersion between parallel planes, solute particles located initially upon such streamlines may only move away from them through molecular diffusion. A similar analysis may be made for particles located initially halfway between the walls in high velocity regions of the profile and which may reach the walls only through molecular diffusion. Also, the orientation of the local flow velocity is always close to that of the mean flow as will be seen below. In the next section, we discuss on the contrary macrodispersion due to variations in the plane of the fracture of the local velocities (averaged this time over the gap).

6. Macrodispersion in the Model Fractures

6.1. Flow Structure and Mean Front Profile

[25] As pointed out above, the complementary rough walls of the fracture model are translated relative to each other in the direction y perpendicular to the mean flow (along the x axis): in this configuration, large-scale channels parallel to x appear [*Gentier et al.*, 1997; *Drazer et al.*, 2004; *Auradou et al.*, 2005] with only weak variations of the flow velocity along their length [*Auradou et al.*, 2006]. In the following, we use a simple model in which the fracture is described as a set of independent parallel channels where the effective flow velocity $U(y)$ depends only on the transverse coordinate.

[26] The validity of this assumption is tested in Figure 6 in which the values of the normalized transit time $\overline{t(x,y)}U/x$ are represented as gray levels at all points (x, y) inside the field of view; $\overline{t(x,y)}$ is the local effective transit time determined by fitting the curve of Figure 3 corresponding to point (x, y) by solutions of equation (7). Dark (light) pixels mark points where $\overline{t(x,y)}U/x$ is respectively higher (lower) than 1: dark and light streaks globally parallel to x are clearly visible and extend over the full length of the model fractures. These streaks correspond to slow (fast) flow paths and their orientation deviates only slightly from x: this is in agreement with the above simple model of parallel flow paths with different velocities remaining correlated along the full path length.

[27] Another important feature of the maps of $\overline{t(x,y)}$ is that they allow one to determine an instantaneous front profile $x_f(y, t)$ at a given time t: in the following, it will be defined as the set of all points for which $\bar{t}(x, y) = t$. In our experiments, this profile was very close to the set of points for which $c(x, y, t)/c_0 = 0.5$ (as can be seen in Figure 2): the determination using the values of $\overline{t(x,y)}$ is however easier and more robust and was used for this reason. In the following, the macrodispersion process is directly characterized by the variations of these front profiles with time without analyzing extensively the concentration maps. Using this procedure allows in addition to remove the effect of Taylor dispersion on the global front spreading, making it easier to determine the macrodispersion component.

6.2. Global Front Dynamics

[28] Figure 7 displays several front profiles obtained at different times by this procedure. As expected, the profile is initially quite flat but large structures appear and grow with time. A key feature is the fact that similar structures are

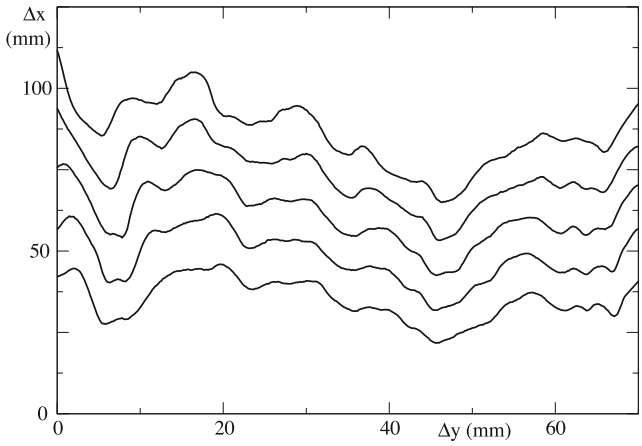

Figure 7. Front profiles $x_f(y, t)$ at times t = 6.5, 8, 9.5, 11, and 12.5 min for a 1000 ppm polymer solution and U = 0.014 mm/s (Pe = 150). The mean flow velocity is oriented from the bottom to the top.

observed on all fronts: it is only their size parallel to the mean flow that increases with time. This confirms the large correlation length parallel to x of the high- and low-velocity regions and therefore the flow channelization already assumed above.

[29] In such cases, as pointed out by *Drazer et al.* [2004], the size of the structures of the front, and therefore its global width $\sigma(t)$ should increase linearly with distance (and time). In the following, the width $\sigma(t)$ is defined by $\sigma^2(t) = < (x_f(y, t) - < x_f(y, t) >_y)^2 >_y$ in which $< x_f(y, t) >_y$ is the mean distance of the front from the inlet at time t: as shown in the inset of Figure 8, $\sigma(t)$ increases as expected linearly with time. Since the mean distance $< x_f(y, t) >_y$ also increases linearly with time, the ratio $\sigma(t)/< x_f(y,t) >_y$ remains constant and may therefore be used to characterize the magnitude of the macrodispersion. In the framework of the simple model assuming parallel independent channels with different flow velocities, $\sigma(t)$ and $< x_f(y, t) >_y$ are respectively of the order of $\delta U\ t$ and $U\ t$ where δU is the root mean square of the velocity variations between the different channels. Therefore the ratio $\sigma(t)/< x_f(y,t) >_y$ corresponds to $\delta U/U$ of the velocity contrasts inside the fracture (a well known result for stratified media with negligible exchange between layers). In Figure 8, for both Newtonian (η = cst.) and power law ($\eta \propto \dot{\gamma}^{n-1}$) fluids the relative velocity fluctuations $\delta U \propto U$ are expected to be constant with U: $\sigma(t)/\overline{x(t)}$ should therefore be independent of the flow rate Q. Figure 8 displays the variation of $\sigma(t)/\overline{x(t)}$ with the normalized velocity U/U_c where U_c is the crossover velocity between the Newtonian and the shear thinning behaviors already defined in section 5. In Figure 8, the values of $\sigma(t)/< x_f(y,t) >_y$ are averaged over several time intervals and the bars indicate their fluctuations within these intervals.

[30] For $U < U_c$, $\sigma(t)/\overline{x(t)}$ retains a constant value close to 0.05 independent of the polymer concentration which likely corresponds to a Newtonian behavior. For $U < U_c$, $\sigma(t)/\overline{x(t)}$ starts to increase above a same threshold value $U/U_c \simeq 2$ for both solutions and follows then a similar trend. In this domain, the shear rate $\dot{\gamma}$ is always zero in the middle of the gap of the fracture and highest at the walls. If the shear rate at the wall is larger than the transition value $\dot{\gamma}_0$ (see section 5), there are two domains in the velocity profile: the fluid rheology is Newtonian in the central part of the fracture and non-Newtonian near the walls [*Gabbanelli et al.*, 2005]. When the flow rate Q increases, the fraction of the flow section where flow is Newtonian shrinks while the fraction where it is non-Newtonian expands.

[31] In the very high velocity limit ($U \gg U_c$), almost all the flow will become non-Newtonian and one may assume that the fluid has a power law rheological characteristic ($\mu \propto \dot{\gamma}^{n-1}$). Then, the average velocity in a given flow channel, i.e., the integral of the velocity profile over the fracture gap, varies faster with the longitudinal pressure gradient ∇p and the gap a (as $\nabla p^{1/n}\ a^{1+1/n}$) than for Newtonian fluids (as $\nabla p\ a^2$). Assuming that all parallel channels are subject to the same pressure gradient and that the normalized standard deviation of their apertures is small ($\sigma(a)/\bar{a} \ll 1$) leads to the estimation of the relative velocity fluctuations $\delta U/U \approx (1 + 1/n)\sigma(a)/\bar{a}$. This will also be the order of magnitude of the relative front width $\sigma(t)/\bar{a}(t)$ at a time t. This value should be related to the value $\sigma_N(t)/\bar{x}_N(t)$ for a Newtonian fluid (n = 1) by:

$$\frac{\sigma(t)/\bar{x}(t)}{\sigma_N(t)/\bar{x}_N(t)} = \frac{1+n}{2n} \tag{8}$$

At very high flow rates, one may therefore expect $\sigma(t)/\overline{x(t)}$ to reach a constant limiting value related to the value for a Newtonian fluid by equation (8) and increasing with the polymer concentration (when n decreases). Using for $\sigma_N(t)/\bar{x}_N(t)$ the value 0.06 obtained in the low-velocity limit (solid line in Figure 8) and for n the values from Table 1 leads to $\sigma(t)/\overline{x(t)}$ = 0.11 and $\sigma(t)/\overline{x(t)}$ = 0.145 respectively for the 500 ppm and 1000 ppm solutions (dotted and dashed horizontal lines). These limits are slightly higher than the

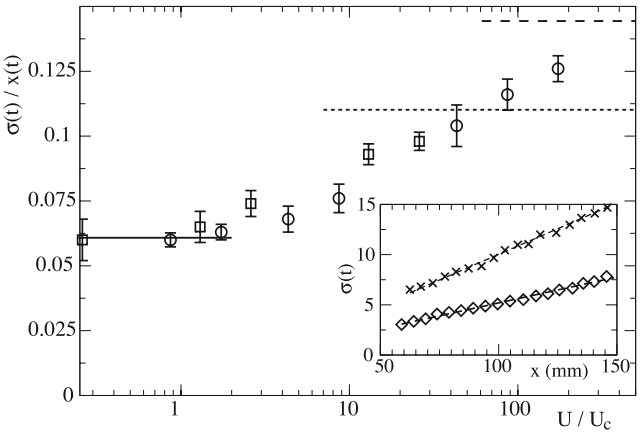

Figure 8. Variation in log linear coordinates of the relative front width $\sigma\ (t)/\overline{x(t)}$ with the normalized mean velocity U/U_c; crossover velocity U_c = 0.01 mm/s and 0.003 mm/s for 500 ppm (squares) and 1000 ppm (circles) solutions. Solid line shows the mean of the data in the low-velocity limit. Dotted and dashed horizontal lines show predicted values for power law fluids with same index n as the 500 ppm and 1000 ppm solutions, respectively. Inset shows variation of $\sigma\ (t)$ (mm) with the distance x for a 1000 ppm solution: diamonds, U = 0.0056 mm/s (Pe = 60); crosses: U = 0.056 mm/s (Pe = 600); dashed line, linear regression.

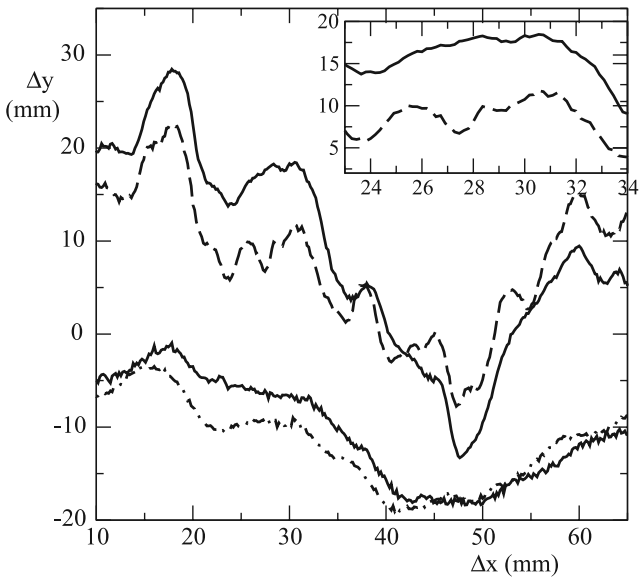

Figure 9. Front geometries for a mean distance from the inlet equal to half the fracture length. Solid (dashed) lines show 1000 ppm (500 ppm) solutions. Top (bottom) lines show $U = 0.3$ mm/s, i.e., $Pe = 3000$ ($U = 0.003$ mm/s, i.e., $Pe = 30$). The two sets of lines have been shifted to allow for easier comparisons. Inset shows close-up of the top curves ($U = 0.3$ mm/s, i.e., $Pe = 3000$).

experimental values at the highest flow velocities. One can therefore assume that the intermediate velocity domain where $\sigma(t)/\overline{x(t)}$ increases with U/U_c corresponds to a transition between Newtonian and non-Newtonian flows.

[32] Let us finally point out that, since this macrodispersion and the local Taylor dispersion described above have a different dependence on distance and flow velocity, it is difficult to compare their magnitudes. Overall, at large distances, the influence of macrodispersion is generally larger although Taylor dispersion remains always sizable.

6.3. Front Geometry

[33] In section 6.2 the overall front width has been shown to depend on the global flow rate and on the fluid rheology; their influence on the detailed front structure will now be analyzed. Figure 9 compares front geometries observed for the two solutions used in the experiments at the lowest (highest) mean velocities investigated: $U = 0.003$ mm/s (0.3 mm/s). The lower velocity is below U_c and the rheology of both fluids is therefore Newtonian. The polymer concentration plays then a minor part and the front geometries are very similar (lower curves). In addition, at this mean velocity, the Péclet number is ≈ 3 and therefore lower than the value $Pe \simeq 14.5$ (see section 5) corresponding to the crossover between Taylor dispersion and longitudinal molecular diffusion. As a result, transport at the local scale is controlled by molecular diffusion which smears out the effect of local velocity fluctuations and smooths the front geometry.

[34] The higher velocity $U = 0.3$ mm/s (top curves) is well above U_c: the global front width increases then with the polymer concentration (see section 6.2), as can be seen for the two top curves in Figure 9. However, at smaller length scales, the geometrical characteristics of the front and their dependence on the fluid rheology are more complex. Geometrical features of lateral size below 10 mm have, for instance, a larger extension parallel to the mean flow for the 500 ppm solution.

[35] Previous theoretical, experimental and numerical studies of displacement fronts between sheared complementary self-affine walls indicate that their geometry is also self-affine (over a finite range of length scales) with the same characteristic exponent ζ as the fracture walls [*Roux et al.*, 1998; *Drazer et al.*, 2004; *Auradou et al.*, 2001]. This implies that the analysis of the front may, in turn, provide useful information on the multiscale geometry of the fracture walls and of the aperture field. Such self-affine profiles $y(x)$ may be characterized quantitatively from the maximum variation $y_{max} - y_{min}$ of $y(x)$ in a window of width Δx (y_{max} and y_{min} are the maximum and minimum values of $y(x)$ in this window.) In this "min-max" method, the average $\Delta y(\Delta x)$ of the values of $y_{max} - y_{min}$ is computed for all locations of the window inside the profile and the process is repeated for the different values of Δx. For a self-affine curve of characteristic roughness exponent ζ_f, one has, for instance, $\Delta y \propto \Delta x^{\zeta_f}$ ($\zeta_f = 1$ corresponds to a Euclidian curve.)

[36] This result is verified in the inset of Figure 10 where the ratio $\Delta y/\Delta x^{\zeta_f}$ is plotted as a function of Δx in log-log coordinates for $\zeta_f = 0.8$: $\Delta y/\Delta x^{\zeta_f}$ is indeed observed to remain constant over a broad range of variation of Δx. The lower boundary of this self affine domain increases slightly with the polymer concentration from ≈ 3 mm (500 ppm) to ≈ 5 mm, (1000 ppm) and depends weakly on the flow velocity (provided $Pe \gtrsim 14$). For Δx below this crossover length, the slope of the curves is close to 0.2, reflecting an Euclidean geometry with $\Delta y \propto \Delta x$.

[37] In order to analyze the influence of the fluid properties and of the flow velocity U on these results, the variation of the ratio $\Delta y/\Delta x$ with Δx is displayed in Figure 10 for the two polymer solutions and for two different values of U ($U < U_c$ and $U > U_c$). The maximum

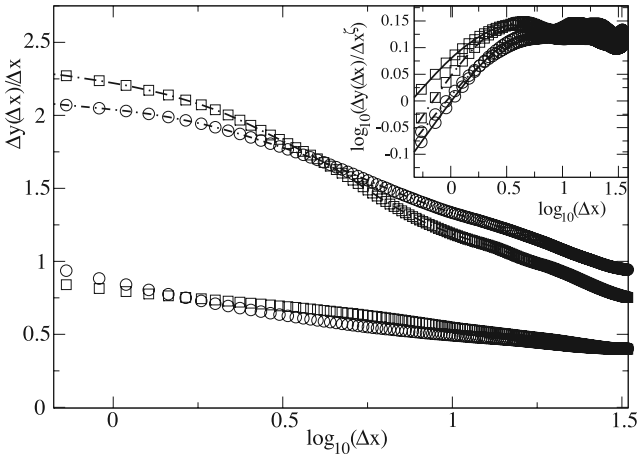

Figure 10. Variation of the ratio $\Delta y(\Delta x)/\Delta x$ as a function of $log_{10}(\Delta x)$ for the same fronts as in Figure 9 with 1000 ppm (circles) and 500 ppm (squares) polymer solutions. Symbols with solid lines show $U = 0.03$ mm/s ($Pe = 300$), and symbols with dotted lines show $U = 0.3$ mm/s ($Pe = 3000$). Inset shows variation of log_{10} ($\Delta y/\Delta x^{\zeta_f}$) as a function of $\log_{10}$ (Δx) with $\zeta_f = 0.8$.

height difference Δy has been normalized by the window width Δx to reduce the amplitude of the global variations of Δy and make more visible the differences between the curves.

[38] For the lowest velocity U, the curves are similar for both polymer concentrations (as expected for a Newtonian rheology). For $U > U_c$ (top curves in Figure 10), the ratio $\Delta y/\Delta x$ increases, reflecting a higher amplitude of the geometrical features of the front at all length scales. In addition to this global trend, the variation of Δy with Δx depends however significantly on the polymer concentration. Features of the front with large transverse sizes Δx are of larger amplitude Δy for the more concentrated solution; on the contrary, smaller features corresponding to low Δx values are more developed for the less concentrated solution (this is qualitatively visible on Figure 9). The two curves cross each other for $\Delta x \approx 4$ mm. This attenuation of small-scale features of the front for the more concentrated solution may reflect an enhancement of the transverse diffusion of the fluid momentum due to its higher viscosity (in other words, drag forces between parallel layers of fluid moving at different velocities become larger). This smooths out both the local velocity gradients and the associated small features of the front but does not influence large-scale velocity variations.

7. Discussion and Conclusion

[39] Studying miscible displacement processes by an optical method in a transparent model fracture has revealed important characteristics of flow and transport in rough fractures: these results may be applicable to fluid displacements and transport in fractured reservoirs. A major feature of this approach is the possible simultaneous analysis of both local mixing and global front spreading due to large-scale heterogeneities: the different transport mechanisms may in particular be characterized by maps of the local transit time from the inlet and of the local dispersion coefficient.

[40] The multiple length scales features of natural fractures have been reproduced by assuming rough walls of complementary self-affine geometries and with a relative displacement parallel to their mean plane, modeling the effect of shear during fracturing. In the present experiments, this relative displacement was perpendicular to the mean flow: this induced a channelization of the flow field with small velocity variations along the streamlines and larger ones across them. Large macrodispersion effects are observed in such a geometry: in the present experiments, the front width increases linearly with distance from the inlet and its structure reflects closely the velocity variations between the different parallel channels. Taking into account the very large correlation length of the velocity along the channels and the low amount of transverse diffusive exchange; this convective front spreading regime may be considered as valid all along the sample length and no transition toward a diffusive regime is to be expected.

[41] In contrast, front spreading at the local scale remains diffusive and the corresponding dispersion coefficient is close to that estimated for Taylor dispersion in an Hele-Shaw cell with plane walls separated by a distance equal to the main aperture of the fracture. This value may however be locally increased by transverse diffusion in highly distorted regions of the fronts where the front gets locally parallel to the mean flow.

[42] These fluid displacements are strongly influenced by the rheology of the flowing fluids and, for the solutions used in the present work, they depend on the polymer concentration and/or the shear rate $\dot{\gamma}$. More precisely, below a transition value $\dot{\gamma}_0$, the polymer solutions used in the present work behave like Newtonian fluids and their concentration has no effect at low mean velocities ($U < U_c$). At higher shear rates ($U > U_c$), the shear thinning effects become significant: they increase with the polymer concentration but may be very different depending on the scale of observation. The global width Δx of the front parallel to the mean flow gets larger at higher polymer concentrations while, in contrast, smaller geometrical features of the front are reduced. In addition, for $U > U_c$, polymers also influence Taylor dispersion at the local scale: in contrast with macrodispersion, this dispersion component is reduced by the flattening of the flow profile between the fracture walls for shear thinning fluids. Using solutions of different polymer concentrations may then allow one to separate these two front spreading mechanisms which vary in opposite directions when the polymer concentration changes. Also, the enhancement of macrodispersion by the shear thinning properties may allow to detect large-scale heterogeneities associated to weak permeability contrasts. These effects may help understand better enhanced recovery processes in which polymer solutions are injected to displace oil or other fluids with a better efficiency.

[43] Such results raise a number of questions to be answered in future work. First, one may expect the spatial correlations of the velocity to decay with distance, leading finally to normal Fickian dispersion. The present samples were not long enough to allow for the observation of this transition: it may however be more easily observable for models designed so that flow is parallel to the relative shear of the complementary fracture surfaces (in this case, the correlation length should be smaller). Another important issue is the influence of contact area on the transport process: one may expect in this case the development of low-velocity regions leading to anomalous dispersion curves.

[44] **Acknowledgments.** We are indebted to G. Chauvin and R. Pidoux for their assistance in the realization of the experimental setup and to C. Allain for her cooperation and advice. H.A. and J.P.H. are funded by the EHDRA (European Hot Dry Rock Association) in the framework of the STREP Pilot plan program (SES6-CT-2003-502706) and by the CNRS-PNRH program. This work was also supported by a CNRS-Conicet Collaborative Research grant (PICS 2178) and by the ECOS Sud program (A03E02). One of us (A.B.) is supported by a doctorate fellowship from the University of Buenos Aires.

References

Adler, P. M., and J.-F. Thovert (1999), *Fractures and Fracture Networks*, Springer, New York.

Aris, R. (1956), On the dispersion of a solute particle in a fluid moving through a tube, *Proc. R. Soc. London, Ser. A*, *235*, 67–77.

Auradou, H., J. P. Hulin, and S. Roux (2001), Experimental study of miscible displacement fronts in rough self-affine fractures, *Phys. Rev. E*, *63*, 066306.

Auradou, H., G. Drazer, J. P. Hulin, and J. Koplik (2005), Permeability anisotropy induced by a shear displacement of rough fractured walls, *Water Resour. Res.*, *40*, W09423, doi:10.1029/2005WR003938.

Auradou, H., G. Drazer, A. Boschan, J. P. Hulin, and J. Koplik (2006), Shear displacement induced channelization in a single fracture, *Geothermics*, *35*, 576–588.

Bear, J. (1972), *Dynamics of Fluids in Porous Media*, 764 pp., Elsevier, New York.

Becker, M., and A. Shapiro (2000), Tracer transport in fractured crystalline rock: Evidence of nondiffusive breakthrough tailing, *Water Resour. Res.*, *36*, 1677–1686.

Berkowitz, B. (2002), Characterizing flow and transport in fractured geological media: A review, *Adv. Water Resour.*, *25*, 861–884.

Bird, R. B., R. C. Armstrong, and O. Hassager (1987), *Dynamics of Polymeric Liquids*, vol. 1, 2nd ed., John Wiley, Hoboken, N. J.

Boschan, A., V. J. Charette, S. Gabbanelli, I. Ippolito, and R. Chertcoff (2003), Tracer dispersion of non-Newtonian fluids in a Hele-Shaw cell, *Physica A*, *327*, 49–53.

Bouchaud, E. (2003), The morphology of fracture surfaces: A tool for understanding crack propagation in complex materials, *Surf. Rev. Lett.*, *10*, 797–814.

Brown, S., A. Caprihan, and R. Hardy (1998), Experimental observation of fluid flow channels in a single fracture, *J. Geophys. Res.*, *103*, 5125–5132.

Detwiler, R., H. Rajaram, and R. J. Glass (2000), Solute transport in variable aperture fractures: An investigation of the relative importance of Taylor dispersion and macrodispersion, *Water Resour. Res.*, *36*, 1611–1625.

Drazer, G., and J. Koplik (2002), Transport in rough self-affine fractures, *Phys. Rev. E*, *66*, 026303.

Drazer, G., H. Auradou, J. Koplik, and J. P. Hulin (2004), Self-affine fronts in self-affine fractures: Large and small-scale structure, *Phys. Rev. Lett.*, *92*, 014501.

Fadili, A., P. Tardy, and A. Pearson (2002), A 3D filtration law for power-law fluids in heterogeneous porous media, *J. Non Newtonian Fluid Mech.*, *106*, 121–146.

Feder, J. (1988), *Fractals, Physics of Solids and Liquids*, Springer, New York.

Gabbanelli, S., G. Drazer, and J. Koplik (2005), Lattice-Boltzmann method for non-Newtonian (power law) fluids, *Phys. Rev. E*, *72*, 046312.

Gentier, S., E. Lamontagne, G. Archambault, and J. Riss (1997), Anisotropy of flow in a fracture undergoing shear and its relationship to the direction of shearing and injection pressure, *Int. J. Rock Mech. Min. Sci.*, *34*(3-4), 94.e1–94.e12.

Horobin, R. W., and J. A Kiernan (Eds.) (2002), *Conn's Biological Stains: A Handbook of Dyes, Stains and Fluorochromes for Use in Biology and Medicine*, Taylor and Francis, Philadelphia, Pa.

Ippolito, I., E. J. Hinch, G. Daccord, and J. P. Hulin (1993), Tracer dispersion in 2-D fractures with flat and rough walls in a radial flow geometry, *Phys. Fluids A*, *5*(8), 1952–1961.

Ippolito, I., G. Daccord, E. J. Hinch, and J. P. Hulin (1994), Echo tracer dispersion in model fractures with a rectangular geometry, *J. Contam. Hydrol.*, *16*(8), 1952–1961.

Kitanidis, P. K. (1997), *Introduction to Geostatistics: Applications in Hydrogeology*, 249 pp., Cambridge Univ. Press, New York.

Matheron, G., and G. de Marsily (1980), Is transport in porous media always diffusive? A counterexample, *Water Resour. Res.*, *16*, 901–917.

NAS Committee on Fracture Characterization and Fluid Flow (1996), *Rock Fractures and Fluid Flow: Contemporary Understanding and Applications*, Natl. Acad. Press, Washington, D. C.

Neretnieks, I., T. Eriksen, and P. Tahtinen (1982), Tracer movement in a single fissure in granite rock: Some experimental results and their interpretation, *Water Resour. Res.*, *18*, 849–858.

Roux, S., F. Plouraboué, and J. P. Hulin (1998), Tracer dispersion in rough open cracks, *Transp. Porous Media*, *32*, 97–116.

Sahimi, M. (1993), Nonlinear transport processes in disordered media, *AIChE J.*, *39*(3), 369–386.

Shah, C. B., and Y. C. Yortsos (1995), Aspects of flow of power-law fluids in porous media, *AIChE J.*, *41*(5), 1099–1112.

Taylor, G. I. (1953), Dispersion of soluble matter in solvent flowing slowly through a tube, *Proc. R. Soc. London, Ser. A*, *219*, 186–203.

Tsang, Y. W., and C. F. Tsang (1987), Channel model of flow through fractured media, *Water Resour. Res.*, *23*(3), 467–479.

Vartuli, M., J.-P. Hulin, and G. Daccord (1995), Taylor dispersion in a polymer solution flowing in a capillary tube, *AIChE J.*, *41*(7), 1622–1628.

Yeo, I. W., M. H. De Freitas, and R. W. Zimmerman (1998), Effect of shear displacement on the aperture and permeability of a rock fracture, *Int. J. Rock Mech. Min. Sci.*, *35*(8), 1051–1070.

H. Auradou, A. Boschan, and J. P. Hulin, Laboratoire Fluides, Automatique et Systèmes Thermiques, Bâtiment 502, Université Paris Sud, F-91405 Orsay Cedex, France. (hulin@fast.u-psud.fr)

R. Chertcoff and I. Ippolito, Grupo de Medios Porosos, Facultad de Ingeniería, Universidad de Buenos Aires, Paseo Colón 850, 1063 Buenos Aires, Argentina.